Nanoscale

Check for updates

Tracking sodium migration in TiS$_2$ using *in situ* TEM†

Bo Han,[a,b] Shulin Chen,[b,c] Jian Zou, [ID][d] Ruiwen Shao,[b] Zhipeng Dou,[b,e] Chen Yang,[f,g] Xiumei Ma,[b] Jing Lu,[f,g] Kaihui Liu, [ID][f,h] Dapeng Yu,[b,f,h,i] Liping Wang, [ID] *[d] Haicheng Wang*[a] and Peng Gao [ID] *[b,h,j]

For alkali-metal ion batteries, revealing the phase transformation and the ion migration dynamics in the electrodes is vital for understanding how the electrodes work and thereby how we can improve them. Here, using *in situ* transmission electron microscopy, we track the structural evolution and migration dynamics during sodium insertion into TiS$_2$ nanostructures with the lattice fringe resolution. We find that the sodiation process of TiS$_2$ is initiated by an intercalation reaction and followed by a conversion reaction. From the same reaction event, the velocity of intercalation/conversion phase boundary migration is found to be ~1.0–1.7 nm s^{-1}, while the pristine/intercalation phase boundary migrates at a velocity of ~2.5 nm s^{-1}. The sodium migration leads to structural fracture to form nanometer-sized domains (~3 nm) with volume expansion. During migration, Na prefers to transport along specific directions. Furthermore, a superstructured Na$_{0.25}$TiS$_2$ intermediate phase with ordered Na ions occupied within the (0001) plane is formed at the reaction front, which is different from the common staging phase. These findings help us understand the working principle and the failure mechanism of the sodium ion battery and also provide useful insights into the general ionic doping of transition metal dichalcogenides.

Introduction

Lithium-ion batteries (LIBs) have been widely applied in portable electronic devices.[1–4] However, the uneven distribution of lithium on Earth's crust and its limited natural abundance restrict its further applications in large-scale

[a]*National Center for Materials Service Safety, University of Science and Technology Beijing, Beijing 100083, China. E-mail: hcwang@mater.ustb.edu.cn*
[b]*Electron Microscopy Laboratory, School of Physics, Peking University, Beijing 100871, China. E-mail: p-gao@pku.edu.cn*
[c]*State Key Laboratory of Advanced Welding and Joining, Harbin Institute of Technology, Harbin 150001, China*
[d]*School of Materials and Energy, State Key Laboratory of Electronic Thin Film and Integrated Devices, University of Electronic Science and Technology of China, Chengdu 610054, China. E-mail: lipingwang@uestc.edu.cn*
[e]*Key Laboratory for Micro-/Nano-Optoelectronic Devices of Ministry of Education, School of Physics and Electronics, Hunan University, Changsha 410082, China*
[f]*State Key Laboratory for Artificial Microstructure & Mesoscopic Physics, School of Physics, Peking University, Beijing 100871, China*
[g]*Academy for Advanced Interdisciplinary Studies, Peking University, Beijing 100871, China*
[h]*Collaborative Innovation Center of Quantum Matter, Beijing 100871, China*
[i]*Shenzhen Key Laboratory of Quantum Science and Engineering, Shenzhen 518055, China*
[j]*International Center for Quantum Materials, School of Physics, Peking University, Beijing 100871, China*
†Electronic supplementary information (ESI) available. See DOI: 10.1039/c9nr00483a

energy storage fields such as power grid storage and electric vehicles. Therefore, the development of new battery systems other than LIBs is necessary. Na-Ion batteries (NIBs) have recently attracted much attention[5–8] due to the low cost, large reserves, wide distribution, less toxicity and environmentally friendly properties of sodium.[9–11] In particular, it has been recently demonstrated that sodium ion batteries can also be used to power electric vehicles.[12] However, finding suitable electrode materials to achieve high power and high capacity is still the main challenge. Compared with LIBs, NIBs are more likely to suffer from voltage hysteresis and relatively poor rate capability due to the larger mass and radius of sodium.[5] Therefore, some high-performance electrode materials in LIB systems are no longer appropriate for NIBs. As an example, graphite is commonly used as an anode in LIBs but the insertion of sodium ions is impossible in conventional carbonate-based electrolyte systems.[13]

Recently, some of the transition metal dichalcogenides (TMDs), which can be generally represented by the layered structure AB$_2$ (A = Mo, Ti, Ta, Hf, W, *etc.*; B = S, Se, Te), were applied as electrode materials for sodium ion batteries.[13–17] Since the B–A–B atomic layers of TMD materials are connected by weak van der Waals forces, TMDs usually have relatively large lattice space along the [0001] direction, which can reversibly accommodate alkali metal ions without excess volume expansion. A host of TMDs, such as MoS$_2$,[14,17] SnS$_2$,[15]

WS$_2$,[16] and low cost TiS$_2$,[18] have been demonstrated to be potential electrode materials in NIB systems due to their good rate property and stable cyclability. In fact, Winn et al.[19] in the 1970s first verified that sodium ions could be electrochemically inserted into the TiS$_2$ host lattice using coulometric titrations, and later in 1980 Newman et al.[20] assembled reversible Na-TiS$_2$ cells at room temperature and observed capacity loss at a high voltage upon cycling. As a promising NIB electrode material, TiS$_2$ has a theoretical specific capacity of 239 mA h g^{-1} for the intercalation electrochemical reaction to form NaTiS$_2$ (i.e., one TiS$_2$ unit cell hosts only one sodium ion). A previous electrochemical study showed that TiS$_2$ demonstrated a specific capacity of 186 mA h g^{-1} at a high current rate of 100 mA h g^{-1} and good cycling stability.[18] To further improve the performance of the TiS$_2$ electrode, revealing the phase transformation and the ion migration behavior is crucial. First-principles calculations[21,22] and nuclear magnetic resonance (NMR) experiments[23,24] suggested that the behavior of alkali ions migration in TiS$_2$ is very different from those in covalent or ionic transition metal oxides with variable valences, mainly due to unique weak van der Waals interactions. In the past decades, a multitude of newly developed techniques including in situ X-ray photoelectron spectroscopy (XPS)[25] and in situ X-ray diffraction (XRD)[26] have been used to clarify the mechanism of the Na-intercalate TiS$_2$ process. The XRD measurement has shown that an unidentified Na$_x$TiS$_2$ phase appeared when TiS$_2$ was discharged to 1.5 V, while other unknown phases formed in the fully discharged electrode at 0.8 V.[27] However, these commonly used bulk-based techniques collecting information from a large area cannot reveal the intermediate and/or localized phases during reactions, which, indeed, were proposed to exist during alkali ion intercalation within TiS$_2$.[28]

Here, the phase transformation and dynamic behavior of sodium ion migration in TiS$_2$ electrode materials is tracked by using high resolution in situ transmission electron microscopy (in situ TEM).[29–34] We find that the insertion of Na into TiS$_2$ is initiated by an intercalation reaction and then followed by a conversion reaction. The velocity of pristine/intercalation phase boundary migration is ~2.5 nm s^{-1}, which is typically larger than the velocity of intercalation/conversion phase boundary migration, which is ~1.0–1.7 nm s^{-1}. Sodium ion insertion leads to the formation of nanosized Na$_{0.25}$TiS$_2$ domains with local structure ordering, i.e., alternate Na and vacancies within every (0001) plane is detected in the intermediate Na$_{0.25}$TiS$_2$ phase, which is distinct from the common staging phase that consists of Na and vacancy (0001) plane. The formation of structure ordering is possibly triggered by the existence of the considerable elastic strain induced by sodium ion intercalation and delicate repulsive interactions between them. However, the intermediate superstructured Na$_{0.25}$TiS$_2$ has not been observed from the ex situ experiments, indicating that in situ TEM probing with high spatial resolution and temporal resolution can be very useful in acquiring information on the structural evolution and ionic migration behavior in solids.

Experimental section

In situ TEM experiment

TiS$_2$ nanosheets were mechanically exfoliated from a single crystal TiS$_2$ by using an adhesive tape and then transferred onto a half TEM bare copper grid (without carbon films) by scratching. The Cu grid was home-cut in an argon-filled glove box. The copper grid with TiS$_2$ acted as a working electrode. The sodium metal was scratched by a tungsten tip acting as a counter electrode. All of the components were assembled in an electrical TEM specimen holder (PicoFemto) in an argon-filled glove box and then transferred into the TEM chamber. During the transfer, the sodium metal was deliberately exposed to air (~5 s) for coating a thin passivation layer of Na$_2$O on the sodium metal surface (acting as a solid-state electrolyte).[35,36] To achieve the sodiation process, the sodium metal coated with the passivation layer was driven by a piezoelectric ceramic motor to come into contact with the TiS$_2$ nanosheet. A small negative bias (~−2 V) was applied between the tungsten probe and the grounded Cu grid with TiS$_2$ nanostructures to initiate the reactions.

Electrochemical measurements

The commercial TiS$_2$ used for this work was purchased from Alfa Aesar Company. TiS$_2$ (80 wt%), carbon black (10 wt%), polyvinylidene fluoride (PVDF, 10 wt%) and N-methylpyrrolidone (NMP) were used to fabricate the electrode. We mixed the components to prepare a uniform slurry, and then dispersed the slurry onto copper foil, followed by drying at 80 °C for 12 h in a vacuum environment. 1 M NaPF$_6$ was used as the electrolyte, which was prepared by mixing ethylene carbonate (EC) and dimethyl carbonate (EC : DMC = 50 : 50 vol%). Sodium foil and glass fiber were used as the anode and the separator, respectively. The weight of the assembled electrode materials was about 2.0 mg cm^{-2}. 2032 coin cells were manufactured in an argon-filled glovebox (O$_2$ < 0.1 ppm; H$_2$O < 0.1 ppm). The batteries were galvanostatically discharged and charged at a current density of 100 mA g^{-1} using LAND CT2001A cell test apparatus at room temperature.

Data acquisition and analysis

In situ high-resolution TEM images and selected area electron diffraction (SAED) patterns were recorded using a Tecnai F20 microscope equipped with a OneView IS (Gatan) camera, operated at an accelerating voltage of 200 kV. Note that the sodium migration can induce contrast change because of defect formation that changes the diffraction condition. To determine the expansion distance (between the reference position and the edge of the nanosheet) in Fig. 2, frame series were recorded (10 frames per second) to study the subtle change in the contrast between neighbouring frames during the sodiation process. The atomic resolution STEM image was acquired using an aberration-corrected Titan Themis G2 microscope at 80 kV with a beam current of 30 pA, a convergence semi-angle of 25 mrad, and a collection semi-angle snap in the range of 53–260 mrad. Atomistic models were

reproduced using VESTA software. Simulated electron diffraction patterns were obtained using Crystalmaker software. FFT patterns and filtered images were calculated using DigitalMicrograph (Gatan) software. The plots were obtained using Origin 2018.

DFT calculations

We used *ab initio* density functional theory (DFT) to investigate the stability of the $Na_{0.25}TiS_2$ crystal model. The plane-wave basis set and the projector augmented wave (PAW) pseudopotential calculation were used to relax geometry optimization in the Vienna *ab initio* simulation package (VASP) software. The atomic positions are fully optimized underneath the 0.001 eV Å^{-1} maximum force of each atom and the convergence standard of energy on each atom is within 1×10^{-5} eV. In geometric optimizations, the cutoff energy is 500 eV, and the *k*-point mesh is sampled with a separation of about 0.04 Å^{-1} in the Brillouin zone.

Results and discussion

Fig. 1a and b show an atomically resolved high-angle annular dark field scanning transmission electron microscopy (HAADF-STEM) image of the pristine TiS_2 nanosheet on viewing from the [0001] direction, where the Ti atoms are brighter than the S atoms because the HAADF-STEM image is

a *Z*-contrast (*Z* is atomic number) image.[37] The SAED viewing from the [0001] zone axis in Fig. 1c demonstrates a hexagonal symmetric pattern, which is in agreement with the simulated electron diffraction based on the atomistic model shown in Fig. S1† (PDF#15-0853, a = 3.397 Å, b = 3.397 Å, c = 5.691 Å).[38] To observe the Na insertion process in real time, we fabricate a solid-state half-cell using TEM, consisting of a TiS_2 nanosheet, metal sodium counter electrode and Na_2O passivation layer acting as a solid-state electrolyte, as shown in Fig. 1d and Fig. S2.†

The sodium-intercalation-induced structural evolution of the TiS_2 nanosheet is monitored, as shown in Fig. 2a (also see Movie S1†). Na ion insertion can cause lattice distortion and volume expansion. As a result, the strain-induced complex contrast changes during sodiation are observed in the TiS_2 nanosheet from the lower magnification images, as shown in Fig. 2a. The enlarged TEM image in Fig. 2b shows that the pristine TiS_2 nanosheet exfoliated from single-crystal TiS_2 has an ordered stacking structure. Note that such stripes are lattice fringes rather than the Moiré pattern. A reference position is marked to measure the distance between the reference position and the edge of the nanosheet (44.3 nm for pristine). During sodium insertion, the TiS_2 nanosheet begins to swell from 44.3 nm to 71.7 nm (~61.9% in expansion), as shown in Fig. 2c. During this dynamic process, Na insertion breaks the TiS_2 interlayers, forming fractures to release stress and thus accommodate more sodium ions. As a result, the observed
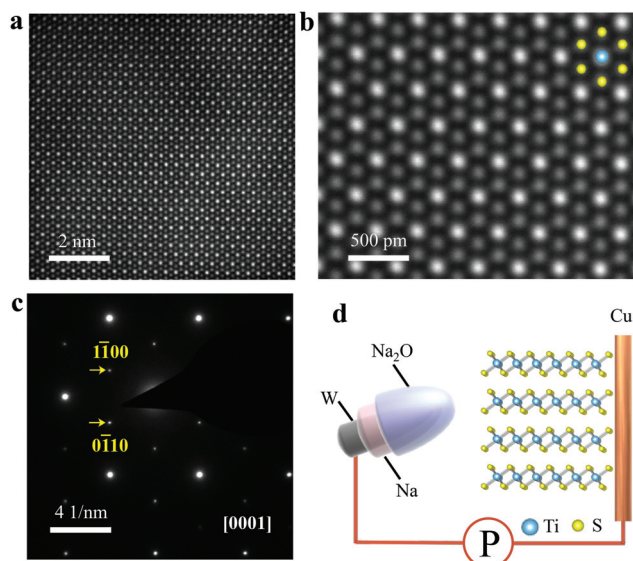

Fig. 1 Tracking sodium ion intercalation in TiS_2 nanosheets in real time. (a) An atomically resolved high angle annular dark field scanning transmission electron microscopy (HAADF-STEM) image of TiS_2 viewed from the [0001] crystal axis. (b) An atomistic model of a TiS_2 unit cell (along the [0001] zone axis) overlaid with the STEM image. Blue: Ti; yellow: S. (c) Selected area electron diffraction (SAED) pattern of the pristine TiS_2 single crystal nanosheet along the [0001] direction. (d) A schematic of the Na–TiS_2 battery cell assembled in TEM consisting of a TiS_2 nanosheet, a metallic sodium probe and a thin passivation layer of Na_2O acting as a solid-state electrolyte.
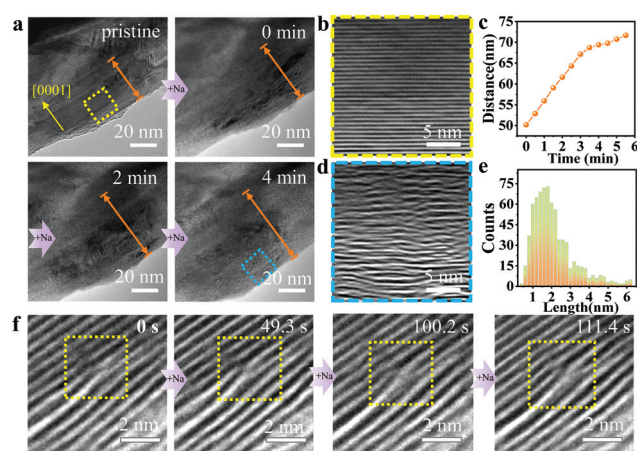

Fig. 2 High-resolution TEM tracking of the structural evolution during Na insertion. (a) Selected high resolution TEM image frames showing lattice expansion during Na intercalation (see also in Movie S1†). (b) An enlarged view of (a) (squared by the yellow dashed line) showing the pristine TiS_2 with a viewing direction nearly perpendicular to the [0001] zone axis. (c) Distance indicated by the orange arrow in (a) is plotted as a function of time, quantitatively illustrating the volume expansion during sodium intercalation. (d) An enlarged view of (a) (squared by the blue dashed line) shows the sodiated TiS_2 interlayer. (e) The measured length of nanometer-sized domains of Na-inserted TiS_2. The mean value is found to be 2.2 ± 1.7 nm. (f) Selected high resolution TEM image series shows the structural evolution of fracture formation. The drift correct areas enclosed by the dashed square highlights the position of the fracture.

volume expansion is significantly larger than the lattice parameter of Na_xTiS_2 ($x \leq 1$) produced by the intercalation mechanism.[39] In each small domain of TiS_2 nanosheets, lattice fringes are well preserved and domains are separated by the fractures. As more sodium ions insert into the TiS_2 nanosheet, ordered layers finally break up into nanometer-sized domains, as shown in Fig. 2d. The lengths of the preserved lattices determine the sizes of domains, which are measured, as shown in Fig. 2e (see Fig. S3† for details). The average domain size is found to be 2.2 ± 1.7 nm. In Fig. 2f, we track the structural evolution of a single fracture formation. During sodium migration, TiS_2 layers start to bend and slide. A straight layer gradually bends and matches with two slid adjacent layers, finally forming a "fork-like" structure at 49.3 s. Such a structural change occurs in all regions where sodium passes

through, finally resulting in the formation of nanometer-sized domains separated by fractures. The formation of high density of fractures can effectively release the strain caused by sodium ion insertion. Note that the lattice expansion is not caused by beam irradiation and column environment (see the details in Fig. S4†).

The high-resolution TEM image series in Fig. 3a–f show the phase boundary propagation during Na insertion into TiS_2 (also see in Movie S2†). At the beginning of the reaction, some wide strips come out, representing the generation of an intercalated Na_xTiS_2 phase with a superstructure, which will be discussed later in detail. Interestingly, there are two interfaces during sodium migration in Fig. 3c, i.e., one interface is between the pristine TiS_2 domain and the sodium intercalated Na_xTiS_2 domain, and the other one is between the intercalated
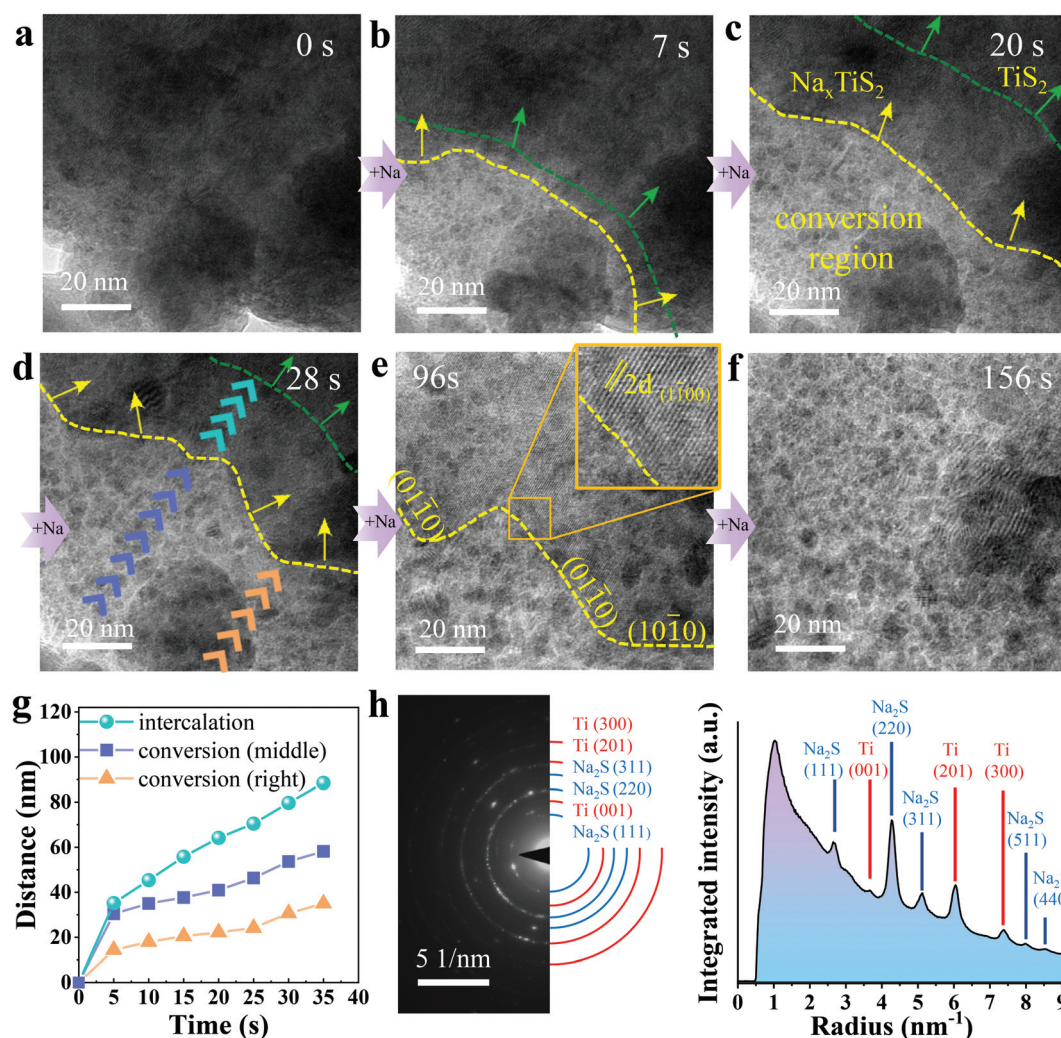

Fig. 3 High-resolution TEM tracking of the Na transport in TiS_2 in real time. (a–f) Selected high resolution TEM image series show phase transformation and phase boundary motion process during Na insertion (see also in Movie S2†). Yellow dashed lines show the boundary between the conversion region and Na_xTiS_2 superstructure region while green dashed lines indicate the interfaces between the superstructure region and initial TiS_2 region. (g) Phase boundary migration distance indicated by sequential arrows in (d) is plotted as a function of time. The intercalation reaction front is marked by cyan. On the conversion reaction front, different positions (two representative points marked by blue and orange, respectively) are in different velocities, due to the anisotropic Na migration. (h) A SAED pattern and the corresponding radial–integral plot of the sodiated TiS_2 electrode of a coin cell battery discharged to 0 V.

domain and the conversion domain. Positions of interfaces at different stages are determined from the images filtered in the Fourier space by including only the lattice plane frequencies of the superlattice, as shown in Fig. S5.† As the reaction proceeds, both of the interfaces gradually move forward but they have different propagation velocities. Based on the positions of interfaces, we can estimate the velocities for both intercalation and conversion reactions. The average migration velocities of the intercalation/conversion phase boundary are found to be ~1.7 nm s^{-1} (middle) and ~1.0 nm s^{-1} (right), while the pristine/intercalation phase boundary migrates at a velocity of ~2.5 nm s^{-1}. The migration velocity of the Na intercalated phase boundary in TiS_2 is lower than that in MoS_2 (~3–7 nm s^{-1}), as reported in the previous work.[33] Although the measured velocity of the phase boundary also depends on the localized contact conditions and can be different from one another, these values still give us some quantitative information on the comparison of relative diffusivity for intercalation and conversion reactions. For both intercalation and conversion, the reaction velocities decrease after 5 s because the potential field near the probe is larger than that away from the probe. As shown in Fig. 3e, the interface between the Na_xTiS_2 domain and the conversion domain prefers to sit in the specific crystal planes {$10\bar{1}0$} likely due to anisotropic barriers for Na transport. After conversion at 156 s, Ti nanoparticles and Na_2S are generated, as shown in Fig. 3f. We also study the reactions in a realistic battery using the *ex situ* TEM method. The sodiated TiS_2 nanosheets from the sodium ion coin battery electrode that is discharged to 0 V verify that the fully discharged products are Na_2S and Ti nanoparticles based on the SAED pattern shown in Fig. 3h and the high-resolution TEM image shown in Fig. S6.†

The structure of the intermediated phase Na_xTiS_2 is also identified below. Fig. 4a shows an enlarged view of the TEM image recorded at 20 s. The lattice-spacing of the super-structure phase (0.588 nm) is twice the lattice-spacing of ($1\bar{1}00$) planes for pristine TiS_2 (0.294 nm). The corresponding fast Fourier transform (FFT) pattern (Fig. 4b) also shows the extra superstructure spots. Based on the FFT filtered image, by only including the superstructure reflections shown in Fig. 4c, the spatial distribution of the Na intercalated super-structure phase and the phase boundary can be determined. From the FFT pattern and high resolution TEM image, the intercalated phase is identified to be every four TiS_2 unit cells host only one sodium ion, *i.e.*, a 2 × 2 ordered superstructure $Na_{0.25}TiS_2$. The simulated electron diffraction pattern (Fig. 4d) of the $Na_{0.25}TiS_2$ phase is in good agreement with the FFT pattern obtained by the experiment. For Na occupation in TiS_2 interlayer, the center sites of sulfur-octahedral has the lowest energy.[40] The atomic structure of $Na_{0.25}TiS_2$ is therefore proposed, as shown in Fig. 4e. Viewing from the [$11\bar{2}0$] direction, one-fourth of the interlayer positions are occupied by sodium ions. The structural stability of the proposed $Na_{0.25}TiS_2$ is further tested and the geometry is also optimized by using density functional theory (DFT) calculations.
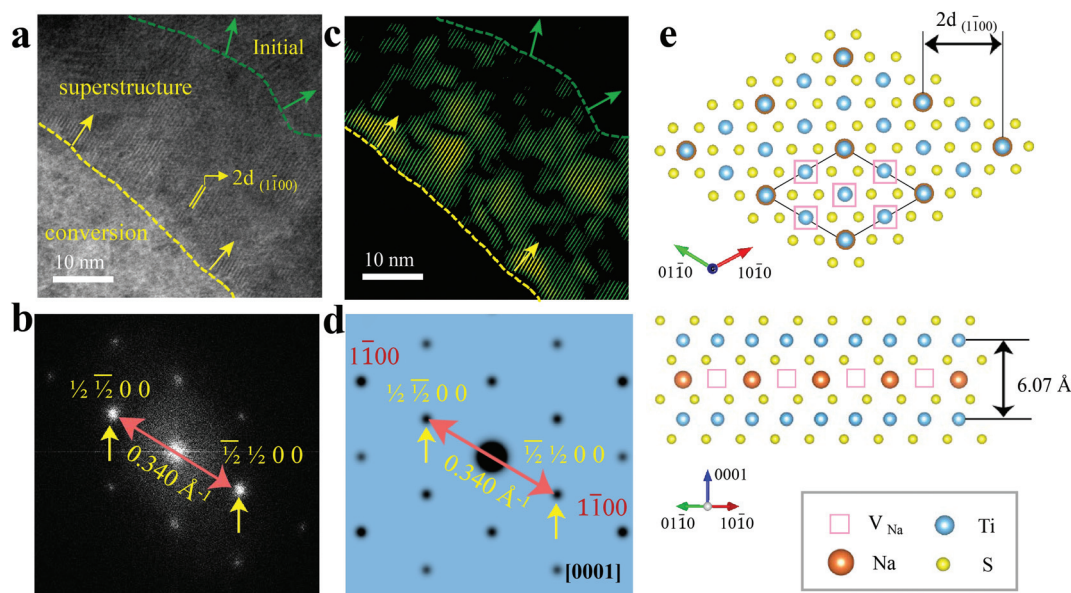

Fig. 4 Superstructure of Na-intercalated TiS_2 during sodiation. (a) An enlarged view of a high resolution TEM image at 21 s during sodiation. Boundaries between the conversion region, Na_xTiS_2 superstructure, and initial region are indicated by yellow and green dashed lines. Arrows show the propagation direction of boundary migration. (b) The FFT pattern of (a); the spacing of superstructure planes are measured (0.340 Å^{-1}) as half of {$1\bar{1}00$} in the simulated diffraction pattern of pristine TiS_2 (0.680 Å^{-1} in Fig. S7b†). (c) A filtered image of (a) by using masks to select $\left(\frac{1}{2}\frac{\bar{1}}{2}00\right)$ and $\left(\frac{\bar{1}}{2}\frac{1}{2}00\right)$ superstructure FFT spots. (d) A simulated electron diffraction pattern of the $Na_{0.25}TiS_2$ superstructure. The viewing direction is [001]. (e) An atomic schematic of the Na intercalated superstructure optimized by DFT calculations, wherein Na, Ti and S atoms are marked with orange, blue, and yellow balls, respectively. Pink squares represent the vacancy between interlayers. One-fourth of the interlayer positions are occupied by sodium ions.

In fact, the local structure ordering in alkali metal ion intercalated van der Waals materials such as K-TiS$_2$[41] and Li-graphite[42,43] has been reported in previous studies. The formation of the superstructure can minimize the elastic strain induced by the sodium intercalation and repulsive interaction between them. These superstructures are called the 'staging phase' consisting of occupied and unoccupied (0001) layers [each (0001) plane is either fully occupied or empty]. However, our observation of the Na$_{0.25}$TiS$_2$ superstructure phase is somehow different from the common staging phase, i.e., Na and vacancy ordering alternate within each (0001) plane. Also, it was reported that Na prefers to locate in hybrid staged hosts with mixed O1–P3 stacking at a low Na concentration (0.2 < x < 0.25), i.e., Na ions simultaneously occupy an octahedral host layer and an adjacent prismatic host layer to form a hybrid.[40] However, in our study, under the dominance of the kinetic behavior, the insertion of Na leads to an O1 ordering intermediate phase instead of the O1–P3 hybrid.

In the case of sodiation in TiS$_2$, the conversion reaction tends to occur depending on the amount of inserted sodium ions. From in situ TEM observation, an intercalation reaction occurs first, which is attributed to the insertion of a small amount of sodium ions. As more sodium ions insert into TiS$_2$, the conversion reaction is then triggered. The ex situ electrochemical characterization studies (Fig. S8†) also confirm such reactions. At the voltage range of 1–3 V, the TiS$_2$ electrode can achieve a specific capacity of 184 mA h g^{-1} via an intercalation mechanism. Once the electrode is discharged to below 1 V, excessive Na ions insert into TiS$_2$, leading to a conversion reaction. Although inserting more Na ions into Na$_x$TiS$_2$ increases the theoretical capacity, the conversion reaction is not fully reversible under real working conditions due to large volume expansion and the formation of an amorphous/nanocrystalline structure, resulting in capacity fade.[44] Furthermore, as shown in the initial discharge profile from ex situ measurements of the Na-TiS$_2$ half battery cell (Fig. S8†), the plateau at 2.1 V represents the intercalation reaction with Na$_x$TiS$_2$ phase generation. However, the Na$_{0.25}$TiS$_2$ phase with ordered sodium ions is not observed, indicating that the kinetic transformation pathways can fundamentally deviate from the equilibrium phase diagram (thermodynamic phase transition), which can help us understand the origin of voltage hysteresis in batteries. In this regard, our in situ observations with high spatial resolution and temporal resolution have the advantage of being able to extract information on the structural evolution and ionic migration behavior in solids.

Conclusions

In summary, we use a high resolution in situ TEM technique to track sodium insertion into the TiS$_2$ nanosheet and both the intercalation reaction and conversion reaction are observed. At the lattice fringe resolution, we discover that the sodium migration in TiS$_2$ leads to volume expansion and structure fracture with the formation of nanosized domains (~3 nm), which

should account for the degraded capacities during the following cycling. The pristine/intercalation phase boundary migrates at a velocity of ~2.5 nm s^{-1}, which is larger than that of intercalation/conversion phase boundary migration (~1.0–1.7 nm s^{-1}). The sodium diffusion is anisotropic, i.e., the interface is preferably along the {10$\bar{1}$0} planes, due to anisotropic diffusion barriers.

The sodium intercalated intermediate phase Na$_{0.25}$TiS$_2$ shows ordering of Na occupation, i.e., within each (0001) plane one-fourth of the unit cells are occupied by sodium to form a 2 × 2 superstructure. The formation of the superstructure can minimize the elastic strain induced by the sodium intercalation and repulsive interaction between them. However, this superstructure is distinct from the common staging phase that consists of Na and vacancy in alternate (0001) planes. From the ex situ experiments, Ti nanoparticles and Na$_2$S generate when the coin cell is fully discharged, which are in good agreement with the in situ TEM results. However, the superstructure phase was not observed when the battery electrode is discharged to 2.1 V, which corresponds to Na$_{0.25}$TiS$_2$, suggesting that the deviation between kinetic transformation pathways and the thermodynamic phase transition is possible. Our direct observations demonstrated in this study can help us understand the migration process of alkali-metal ions in transition metal dichalcogenides and elucidate the design and development of better sodium ion batteries.

Conflicts of interest

There are no conflicts to declare.

Acknowledgements

Notes and references

1 M. Armand and J.-M. Tarascon, Nature, 2008, 451, 652.
2 B. Scrosati, J. Solid State Electrochem., 2011, 15, 1623–1630.
3 R. Service, Science, 2018, 359, 1080.
4 L. Wang, Q. Wang, W. Jia, S. Chen, P. Gao and J. Li, J. Power Sources, 2017, 342, 175–182.
5 M. D. Slater, D. Kim, E. Lee and C. S. Johnson, Adv. Funct. Mater., 2013, 23, 947–958.
6 D. Kundu, E. Talaie, V. Duffort and L. F. Nazar, Angew. Chem., Int. Ed., 2015, 54, 3431–3448.

7 C. Vaalma, D. Buchholz, M. Weil and S. Passerini, *Nat. Rev. Mater.*, 2018, **3**, 18013.

8 J. Liang, F. Li and H. M. Cheng, *Energy Storage Mater.*, 2017, **7**, A1–A3.

9 D. Larcher and J. M. Tarascon, *Nat. Chem.*, 2015, **7**, 19–29.

10 S. Kim, D. Seo, X. Ma, G. Ceder and K. Kang, *Adv. Energy Mater.*, 2012, **2**, 710–721.

11 Y. Wang, R. Chen, T. Chen, H. Lv, G. Zhu, L. Ma, C. Wang, Z. Jin and J. Liu, *Energy Storage Mater.*, 2016, **4**, 103–129.

12 Website: http://www.iop.cas.cn/xwzx/snxw/201806/t20180608_5024146.html.

13 M. M. Doeff, Y. Ma, S. J. Visco and L. C. De Jonghe, *J. Electrochem. Soc.*, 1993, **140**, L169–L170.

14 Z. Hu, L. Wang, K. Zhang, J. Wang, F. Cheng, Z. Tao and J. Chen, *Angew. Chem.*, 2014, **126**, 13008–13012.

15 B. Qu, C. Ma, G. Ji, C. Xu, J. Xu, Y. S. Meng, T. Wang and J. Y. Lee, *Adv. Mater.*, 2014, **26**, 3854–3859.

16 D. Su, S. Dou and G. Wang, *Chem. Commun.*, 2014, **50**, 4192–4195.

17 X. Xie, Z. Ao, D. Su, J. Zhang and G. Wang, *Adv. Funct. Mater.*, 2015, **25**, 1393–1403.

18 Y. Liu, H. Wang, L. Cheng, N. Han, F. Zhao, P. Li, C. Jin and Y. Li, *Nano Energy*, 2016, **20**, 168–175.

19 D. A. Winn, J. M. Shemilt and B. C. H. Steele, *Mater. Res. Bull.*, 1976, **11**, 559–566.

20 G. H. Newman and L. P. Klemann, *J. Electrochem. Soc.*, 1980, **127**, 2097–2099.

21 A. Van der Ven, J. C. Thomas, Q. Xu, B. Swoboda and D. Morgan, *Phys. Rev. B: Condens. Matter Mater. Phys.*, 2008, **78**, 104306.

22 A. Van der Ven, J. Bhattacharya and A. A. Belak, *Acc. Chem. Res.*, 2013, **46**, 1216–1225.

23 M. Wilkening, W. Kuechler and P. Heitjans, *Phys. Rev. Lett.*, 2006, **97**, 065901.

24 M. Wilkening and P. Heitjans, *Phys. Rev. B: Condens. Matter Mater. Phys.*, 2008, **77**, 024311.

25 D. Tonti, C. Pettenkofer and W. Jaegermann, *J. Phys. Chem. B*, 2004, **108**, 16093–16099.

26 B. Tian, W. Tang, K. Leng, Z. Chen, S. J. R. Tan, C. Peng, G.-H. Ning, W. Fu, C. Su, G. W. Zheng and K. P. Loh, *ACS Energy Lett.*, 2017, **2**, 1835–1840.

27 H. S. Ryu, J. S. Kim, J. S. Park, J. W. Park, K. W. Kim, J. H. Ahn, T. H. Nam, G. Wang and H. J. Ahn, *J. Electrochem. Soc.*, 2012, **160**, A338–A343.

28 A. Leblancsoreau, M. Danot, L. Trichet and J. Rouxel, *Mater. Res. Bull.*, 1974, **9**, 191–197.

29 K. He, S. Zhang, J. Li, X. Yu, Q. Meng, Y. Zhu, E. Hu, K. Sun, H. Yun, X. Q. Yang, Y. Zhu, H. Gan, Y. Mo, E. A. Stach, C. B. Murray and D. Su, *Nat. Commun.*, 2016, **7**, 11441.

30 Z. Zeng, X. Zhang, K. Bustillo, K. Niu, C. Gammer, J. Xu and H. Zheng, *Nano Lett.*, 2015, **15**, 5214–5220.

31 H. Xie, X. Tan, E. J. Luber, B. C. Olsen, W. P. Kalisvaart, K. L. Jungjohann, D. Mitlin and J. M. Buriak, *ACS Energy Lett.*, 2018, **3**, 1670–1676.

32 M. E. Holtz, Y. Yu, D. Gunceler, J. Gao, R. Sundararaman, K. A. Schwarz, T. A. Arias, H. D. Abruna and D. A. Muller, *Nano Lett.*, 2014, **14**, 1453–1459.

33 P. Gao, L. Wang, Y. Zhang, Y. Huang and K. Liu, *ACS Nano*, 2015, **9**, 11296–11301.

34 P. Gao, Y.-Y. Zhang, L. Wang, S. Chen, Y. Huang, X. Ma, K. Liu and D. Yu, *Nano Energy*, 2017, **32**, 302–309.

35 J. W. Wang, X. H. Liu, S. X. Mao and J. Y. Huang, *Nano Lett.*, 2012, **12**, 5897–5902.

36 M. Gu, A. Kushima, Y. Shao, J. G. Zhang, J. Liu, N. D. Browning, J. Li and C. Wang, *Nano Lett.*, 2013, **13**, 5203–5211.

37 S. Pennycook and D. Jesson, *Ultramicroscopy*, 1991, **37**, 14–38.

38 I. Oftedal, *Z. Phys. Chem., Stoechiom. Verwandtschaftsl.*, 1928, **134**, 301–310.

39 T. Hibma, *J. Solid State Chem.*, 1980, **34**, 97–106.

40 J. Vinckeviciute, M. D. Radin and A. Van der Ven, *Chem. Mater.*, 2016, **28**, 8640–8650.

41 L. Wang, J. Zou, S. Chen, G. Zhou, J. Bai, P. Gao, Y. Wang, X. Yu, J. Li, Y.-S. Hu and H. Li, *Energy Storage Mater.*, 2018, **12**, 216–222.

42 J. E. Fischer and T. E. Thompson, *Phys. Today*, 1978, **31**, 36–45.

43 W. Rudorff, *Adv. Inorg. Chem.*, 1959, **1**, 223–266.

44 H. Tao, M. Zhou, R. Wang, K. Wang, S. Cheng and K. Jiang, *Adv. Sci.*, 2018, **5**, 1801021.